Journal of Computational Physics ••• (••••) ••••••

Contents lists available at ScienceDirect

Journal of Computational Physics

www.elsevier.com/locate/jcp

A target-fixed immersed-boundary formulation for rigid bodies interacting with fluid flow

Tzu-Yuan Lin, Hsin-Yu Hsieh, Hsieh-Chen Tsai *

Department of Mechanical Engineering, National Taiwan University, Taipei, Taiwan

ARTICLE INFO

Article history:
Received 6 January 2020
Received in revised form 4 August 2020
Accepted 11 November 2020
Available online xxxx

Keywords:
Immersed boundary method
Flow-structure interaction
Body-fixed frame
Rigid-bodies dynamics
Accurate surface stress

ABSTRACT

We present an immersed boundary projection method for flow-structure interaction problems involving rigid bodies with complex geometries. Dynamics of a rigid body interacting with fluid flow and kinematics of other rigid bodies undergoing prescribed motions are coupled implicitly with the incompressible vorticity equations. In particular, the method is formulated in a frame of reference fixed on the rigid body under flow-structure interaction (the target) so that the coupled system can be solved non-iteratively, accurately, and efficiently. The implicit coupling of the fluid solver and dynamics and kinematics of rigid bodies ensures the method being stable for low solid-to-fluid mass ratios. The influence of fictitious fluid inside the rigid body is considered and the spurious oscillations in surface stresses are filtered to impose physically correct rigid body dynamics. Similar to many predecessors of the immersed boundary projection method, the resulting discrete system is solved efficiently using a block-LU decomposition. We then validate the method with two-dimensional test problems of a neutrally buoyant cylinder migrating in a planar Couette flow and a freely falling or rising cylindrical rigid body.

© 2020 Elsevier Inc. All rights reserved.

1. Introduction

The immersed boundary (IB) method was originally proposed by Peskin [1]. The key features of IB method are that the body surface is treated as a boundary immersed in the fluid, and separate grids are used on the fluid and immersed boundary. Two grids communicate through smearing the surface stresses to the Eulerian fluid grid and interpolating the fluid velocity to the Lagrangian immersed boundary grid using a numerical delta function. This feature allows the method to handle objects with complex geometries interacting with fluid flow and obviates the need of computationally expensive tasks, such as re-meshing, since the Eulerian fluid grid does not need to conform with bodies. Taira and Colonius [2] developed a projection formulation of IB method which treats immersed boundary forces as Lagrange multipliers to the no-slip constraints to solve the incompressible flow around rigid bodies with prescribed kinematics. Colonius and Taira [3] further improved the efficiency of the projection method by introducing a null-space approach of the method. The application of the immersed boundary projection method ranges from fundamental problems of airfoil aerodynamics [4–8] and collisions between rigid bodies in fluids [9], to industrial problems in vertical-axis wind turbines [10].

During recent years, the IB method has been extensively developed and applied to flow-structure interaction (FSI) problems of rigid bodies [11–18] and elastic bodies [19–22]. Sotiropoulos and Yang [23] published a review paper on IB methods for FSI discussing coupling of fluid and solid systems. When the motions of fluid and bodies are coupled explicitly or semi-

* Corresponding author.
E-mail addresses: d02522030@ntu.edu.tw (T.-Y. Lin), r06522316@ntu.edu.tw (H.-Y. Hsieh), hsiehchentsai@ntu.edu.tw (H.-C. Tsai).

https://doi.org/10.1016/j.jcp.2020.110003
0021-9991/© 2020 Elsevier Inc. All rights reserved.

Please cite this article as: T.-Y. Lin, H.-Y. Hsieh and H.-C. Tsai, A target-fixed immersed-boundary formulation for rigid bodies interacting with fluid flow, Journal of Computational Physics, https://doi.org/10.1016/j.jcp.2020.110003

implicitly, the coupling is referred as weak coupling; while the fluid and solid governing equations are coupled implicitly, the coupling is called strong coupling. Numerical instabilities caused by the added-mass effect of the fictitious fluid motion inside bodies are observed in IB methods with weak coupling, which become unstable when the solid-to-fluid mass ratio is reduced below a critical value [11,12,14,15]. Although this numerical instability can be improved by using a strong coupling [12] or including information of added mass [13,17], high computational cost is required in general due to iteration. For example, the strongly-coupled IB method proposed by Lācis et al. [18] shows stable simulation for density ratios as low as 10^{-4}.

Kim and Choi [24] also presented a review on the recent developments of IB methods for FSI and discussed relevant issues. In their review paper, IB methods for FSI are further categorized by the way numerical method transfers current-time information between fluid and structure at an interface. Monolithic approach solves the FSI system with one combined solver while partitioned approach couples two separate solvers to advance the FSI system. Partitioned approach with weak coupling [25,26] shows a stability limit in solid-to-fluid mass ratio due to the aforementioned added mass effect of the fictitious fluid motion inside bodies, which can be lowered by introducing appropriate predictors. With appropriate iteration methods, monolithic approach [1,18] and partitioned approach using strong coupling [12,17] show in principle no limitation in simulating the FSI system at low solid-to-fluid density ratios. Although computationally expensive iterations are needed in general, non-iterative IB methods are proposed for FSI problems with rigid bodies. Yang and Stern [16] presented a non-iterative sharp-interface direct-forcing IB method using partitioned approach with strong coupling. The FSI system is simulated in a temporary grid-parallel non-inertial frame following the body motion so that there is no relative motion between the body and the fluid grid and the FSI system can be advanced in time non-iteratively. Lācis et al. [18] introduced a time-lagged interpolation to remove the need for obtaining the position of Lagrangian points a priori.

Many IB methods are observed containing spurious oscillations in surface stresses [27–30], which can result in inaccurate force and torque being exerted on bodies and lead to incorrect body dynamics for FSI problems. Goza et al. [29] have noted that the surface stress oscillations are due to an inaccurate representation of the high frequency components of the surface stresses conveyed by the ill-posedness of an integral equation of the first kind by which surface stresses are solved. They also developed an efficient filtering technique to remove erroneous high-frequency stress components.

In this study, we are interested in developing a non-iterative monolithic-approach IB method to simulate a rigid body under flow-structure interaction (the FSI body) together with a number of other rigid bodies undergo prescribed motions (non-FSI bodies) in the fluid flow. Particularly, inspired by Yang and Stern [16], we simulate the FSI system in a frame of reference fixed on the FSI rigid body of interest (the target) so that the Lagrangian points on the FSI body do not move with respect to the fluid grid. The advantages to simulate the FSI system in the target-fixed frame are that the need of position iterations of the target to advance the FSI system is removed and the FSI forces between the fluids and the FSI body become spatially fixed. In section 2, we formulate the general immersed-boundary fluid equations as well as the equations of motion of the FSI rigid body in the target-fixed frame. The information of added mass of the fictitious fluid motion is included based on Lācis et al. [18] for improving the numerical stability. In section 3, we derive the present IB method in detail. A null-space based fluid solver of Colonius and Taira [3] is used to discretize the target-fixed fluid equations and coupled implicitly with the target-fixed FSI equations of motion to form a discrete linear system of equations. An accurate stress filter introduced by Goza et al. [29] is implemented in the target-fixed FSI equations of motion to impose physically correct surface stresses. Moreover, when spatial integrations involving the FSI forces in the governing equations are integrated over time at temporal discretization, time integrations can be interchanged with spatial integrations because the FSI forces are spatially fixed in the target-fixed frame. As a result, by solving for the time-averaged FSI forces between each time step, those terms involving the FSI forces can be advanced in time exactly without truncation errors. The discrete equations are solved non-iteratively using a block-LU decomposition, which results in an algorithm with five steps. First, predictions are made for both fluid motion and FSI body kinematics in the absence of the surface stresses. Second, a modified Poisson equation is solved for prediction of the surface stresses of the FSI body that enforce the no-slip constraint and rigid body dynamics in the absence of non-FSI bodies. Third, another modified Poisson equation is solved for the surface stresses of non-FSI bodies that enforce the no-slip constraint. Fourth, the surface stresses of the FSI body are corrected through projection. Finally, fluid motion and the FSI rigid body kinematics are updated through another projections. The current method is then validated in section 4 with two tests: a circular cylinder freely falling or rising in fluids, and a neutrally buoyant cylinder migrating in a planar Couette flow.

2. Governing equations

We consider rigid bodies immersed in an unbounded fluid domain Ω and the viscous flow induced by the rigid-body motion is incompressible. The FSI body is modeled by an immersed body Γ_1 and non-FSI bodies are modeled by immersed boundary bodies Γ_2. The system can be subject to a constant background acceleration such as the gravitational acceleration. The FSI body is free to translate and rotate about a center of rotation. The dynamics of the FSI body are under the influence of background acceleration and surface forces exerted by the fluid. Non-FSI bodies undergo prescribed motions in fluids. We have fixed the frame of reference on the FSI body (the target) so that this non-inertial body-fixed frame moves and rotates with time-varying center-of-mass velocity and angular velocity of the FSI body, respectively. In this body-fixed frame of reference (the target-fixed frame), we let $\boldsymbol{x}$ denote the Eulerian coordinate representing a position vector in the fluid domain, $\boldsymbol{\chi}_1(s)$ as the Lagrangian coordinate attached to Γ_1, and $\boldsymbol{\chi}_2(s,t)$ as the Lagrangian coordinate attached to Γ_2, where

s is the variable that parameterizes the body surface. $\boldsymbol{\chi}_1(s)$ does not depend on time due to the target-fixed-fame nature, which leads to spatially-fixed FSI forces and therefore removes the need for iterations to advance the FSI system in time. $\boldsymbol{\chi}_2(s,t)$ is time-dependent because of the relative motions between the FSI body and non-FSI bodies in general.

The dimensionless governing equations of this system are

$$\frac{\partial \boldsymbol{u}}{\partial t} = -\nabla \Pi + [\boldsymbol{u} - \boldsymbol{u}_a(\boldsymbol{x},t)] \times \boldsymbol{\omega} + \frac{1}{Re}\nabla^2 \boldsymbol{u} + \int_{\Gamma_1} \boldsymbol{f}(\boldsymbol{\chi}_1(s),t)\delta(\boldsymbol{\chi}_1(s) - \boldsymbol{x})\, ds + \int_{\Gamma_2} \boldsymbol{f}(\boldsymbol{\chi}_2(s,t),t)\delta(\boldsymbol{\chi}_2(s,t) - \boldsymbol{x})\, ds\,, \tag{1}$$

$$\nabla \cdot \boldsymbol{u} = 0\,, \tag{2}$$

$$\int_{\Omega} \boldsymbol{u}(\boldsymbol{x},t)\delta(\boldsymbol{x} - \boldsymbol{\chi}_1(s))d\boldsymbol{x} = \boldsymbol{u}_s(t) + \boldsymbol{\omega}_s(t) \times \boldsymbol{r}(\boldsymbol{\chi}_1(s))\,, \tag{3}$$

$$\int_{\Omega} \boldsymbol{u}(\boldsymbol{x},t)\delta(\boldsymbol{x} - \boldsymbol{\chi}_2(s,t))d\boldsymbol{x} = \boldsymbol{u}_B(\boldsymbol{\chi}_2(s,t),t)\,, \tag{4}$$

$$M_e\left(\frac{d\boldsymbol{u}_s}{dt} + \boldsymbol{\omega}_s \times \boldsymbol{u}_s\right) = -\int_{\Gamma_1} \boldsymbol{f}(\boldsymbol{\chi}_1(s),t)\, ds + M_e \boldsymbol{a}\,, \tag{5}$$

$$\boldsymbol{I}_e \frac{d\boldsymbol{\omega}_s}{dt} + \boldsymbol{\omega}_s \times (\boldsymbol{I}_e \boldsymbol{\omega}_s) = -\int_{\Gamma_1} \boldsymbol{r}(\boldsymbol{\chi}_1(s)) \times \boldsymbol{f}(\boldsymbol{\chi}_1(s),t)\, ds + M_e(\boldsymbol{r}_c \times \boldsymbol{a})\,, \tag{6}$$

where

$$\Pi = p + \frac{1}{2}|\boldsymbol{u} - \boldsymbol{u}_a(\boldsymbol{x},t)|^2 - \frac{1}{2}|\boldsymbol{u}_a(\boldsymbol{x},t)|^2 + \frac{1}{2}|\boldsymbol{u}_s|^2 - \boldsymbol{a} \cdot \boldsymbol{r}(\boldsymbol{x}), \tag{7}$$

$$\boldsymbol{u}_a(\boldsymbol{x},t) = \boldsymbol{u}_s(t) + \boldsymbol{\omega}_s(t) \times \boldsymbol{r}(\boldsymbol{x})\,, \tag{8}$$

$$M_e = M_s - V_s\,, \tag{9}$$

$$\boldsymbol{I}_e = \boldsymbol{I}_s - \boldsymbol{I}_A\,. \tag{10}$$

First, all vector quantities in equations (1) to (10) are measured in the target-fixed frame. In (1), a simple form of the fluid equation is derived in Appendix A. $\boldsymbol{u}$ and $\boldsymbol{\omega}$ are respectively the dimensionless fluid velocity and vorticity in the inertial laboratory frame. $\boldsymbol{f}$ are the dimensionless immersed boundary stresses exerted by the body on the fluid. Π is the dimensionless modified pressure defined in (7). p is the dimensionless pressure. $\boldsymbol{a}$ is the dimensionless time-varying background acceleration. $\boldsymbol{u}_a$ is the dimensionless velocity of the Eulerian fluid grid defined in (8). $\boldsymbol{r}(\boldsymbol{x})$ is the dimensionless arm from the center of rotation to a point in the fluid domain.

(2) is the incompressibility constraint. (3) shows the no-slip condition for FSI body. Let $\boldsymbol{\chi}_{1,L}$ be the Lagrangian coordinate of the FSI body in the inertial laboratory frame, then

$$\boldsymbol{\chi}_{1,L}(s,t) = \int_0^t \left(\boldsymbol{u}_s(t') + \boldsymbol{\omega}_s(t') \times \boldsymbol{r}(\boldsymbol{\chi}_1(s))\right) dt'\,, \tag{11}$$

where $\boldsymbol{u}_s$ and $\boldsymbol{\omega}_s$ are the dimensionless center-of-mass translational and angular velocities and $\boldsymbol{r}(\boldsymbol{\chi}_1)$ is the dimensionless arm from the center of rotation to a point on Γ_1. Therefore, the time derivative of $\boldsymbol{\chi}_{1,L}$ is composed of the translational and rotational components:

$$\frac{\partial \boldsymbol{\chi}_{1,L}(s,t)}{\partial t} = \boldsymbol{u}_s(t) + \boldsymbol{\omega}_s(t) \times \boldsymbol{r}(\boldsymbol{\chi}_1(s))\,, \tag{12}$$

which gives (3) using the immersed boundary formulation. (4) described the no-slip conditions for non-FSI bodies. The kinematics of non-FSI bodies are prescribed by the dimensionless velocity $\boldsymbol{u}_B(\boldsymbol{\chi}_2(s,t),t)$. After the dynamics of the FSI body are solved at each time step, the motions of the non-FSI bodies relative to the FSI body are determined and $\boldsymbol{\chi}_2(s,t)$ can be pre-computed through time integration.

(5) is the translational equation of motion of the FSI body in the target-fixed frame. Based on Lācis et al. [18], the effect of the fictitious fluid motion inside the rigid body can be taken into account by introducing an effective mass, M_e, as in (9). V_s, and M_s are the dimensionless volume and mass of the FSI body. (6) is the rotational equation of motion of the FSI body in the target-fixed frame. $\boldsymbol{r}_c$ is the dimensionless arm from the center of rotation to the center of mass of the rigid body. Similarly, an effective moment of inertia, $\boldsymbol{I}_e$, is introduced as in (10). $\boldsymbol{I}_A$ and $\boldsymbol{I}_s$ are the dimensionless area moment

of inertia and moment of inertia of the body about the center of rotation. We consider the axes of the target-fixed frame to be aligned with the principal axes of $\boldsymbol{I}_s$, so that $\boldsymbol{I}_s$ is diagonal. If a thin rigid body is considered, then V_s and $\boldsymbol{I}_A$ are equal to zero.

In (1) - (10), $\boldsymbol{r}$, $\boldsymbol{x}$, $\boldsymbol{\chi}_i$, and s were nondimensionalized by a characteristic length scale, L; $\boldsymbol{u}$, $\boldsymbol{u}_s$, and $\boldsymbol{u}_B$ were nondimensionalized by a characteristic velocity scale, U_∞; ∇, V_s, and $\boldsymbol{I}_A$ were nondimensionalized by $1/L$, L^3, and L^5; t was nondimensionalized by L/U_∞; $\boldsymbol{\omega}$ and $\boldsymbol{\omega}_s$ were nondimensionalized by U_∞/L; $\boldsymbol{a}$ was nondimensionalized by U_∞^2/L; M_s was nondimensionalized by $\rho_f L^3$; $\boldsymbol{I}_s$ was nondimensionalized by $\rho_f L^5$; and p and $\boldsymbol{f}$ were nondimensionalized by $\rho_f U_\infty^2$, where ρ_f is the fluid density. The Reynolds number in (1) is defined as $Re = U_\infty L/\nu_f$, where ν_f is the kinematic viscosity of the fluid.

The advantage of formulating the FSI system in the target-fixed frame is that in this frame of reference the FSI Lagrangian points do not move with respect to the Eulerian fluid grid. Therefore, the spatial integrations involving the FSI forces in (1), (5), and (6) can be interchanged with time integrations at temporal discretization (see section 3.2). By solving for the time-averaged FSI forces between each time step, the exact time integrations of those spatial integrations are imposed without truncation errors as the FSI system is advanced in time. The price for this simplicity is that we must now use the Navier-Stokes equations in a body-fixed frame (see (44) in Appendix A) and correct the time derivatives of $M_e\boldsymbol{u}_s$ and $\boldsymbol{I}_e\boldsymbol{\omega}_s$ with their cross products with body angular velocity in (5) and (6). Fortunately, a simple form of (44) derived in Appendix A and corrections to $M_e\boldsymbol{u}_s$ and $\boldsymbol{I}_e\boldsymbol{\omega}_s$ can be easily implemented.

For convenience, we can write the cross product of two vectors $\boldsymbol{a}$ and $\boldsymbol{b}$ in the following matrix operation:

$$\boldsymbol{a} \times \boldsymbol{b} = \boldsymbol{X}(\boldsymbol{a})\boldsymbol{b} = \boldsymbol{X}^T(\boldsymbol{b})\boldsymbol{a} \,, \tag{13}$$

where

$$\boldsymbol{X}(\boldsymbol{a}) = \begin{pmatrix} 0 & -a_3 & a_2 \\ a_3 & 0 & -a_1 \\ -a_2 & a_1 & 0 \end{pmatrix} \tag{14}$$

is a skew-symmetric matrix associated with the vector $\boldsymbol{a} = (a_1, a_2, a_3)^T$. Therefore, (1), (3), (5), (6), and (8) can be written as

$$\frac{\partial \boldsymbol{u}}{\partial t} = -\nabla \Pi + \boldsymbol{X}(\boldsymbol{u} - \boldsymbol{u}_a(\boldsymbol{x}, t))\,\boldsymbol{\omega} + \frac{1}{Re}\nabla^2 \boldsymbol{u} + \int_{\Gamma_1} \boldsymbol{f}(\boldsymbol{\chi}_1(s), t)\delta(\boldsymbol{\chi}_1(s) - \boldsymbol{x})\, ds + \int_{\Gamma_2} \boldsymbol{f}(\boldsymbol{\chi}_2(s,t), t)\delta(\boldsymbol{\chi}_2(s,t) - \boldsymbol{x})\, ds \,, \tag{15}$$

$$\int_\Omega \boldsymbol{u}(\boldsymbol{x}, t)\delta(\boldsymbol{x} - \boldsymbol{\chi}_1(s))d\boldsymbol{x} = \boldsymbol{u}_s(t) + \boldsymbol{X}^T(\boldsymbol{r}(\boldsymbol{\chi}_1(s)))\boldsymbol{\omega}_s(t) \,, \tag{16}$$

$$M_e\left(\frac{d\boldsymbol{u}_s}{dt} + \boldsymbol{X}(\boldsymbol{\omega}_s)\boldsymbol{u}_s\right) = -\int_{\Gamma_1} \boldsymbol{f}(\boldsymbol{\chi}_1(s), t)\, ds + M_e\boldsymbol{a} \,, \tag{17}$$

$$\boldsymbol{I}_e\frac{d\boldsymbol{\omega}_s}{dt} + \boldsymbol{X}(\boldsymbol{\omega}_s)\boldsymbol{I}_e\boldsymbol{\omega}_s = -\int_{\Gamma_1} \boldsymbol{X}(\boldsymbol{r}(\boldsymbol{\chi}_1(s)))\boldsymbol{f}(\boldsymbol{\chi}_1(s), t)\, ds + M_e\boldsymbol{X}(\boldsymbol{r}_c)\boldsymbol{a} \,, \tag{18}$$

$$\boldsymbol{u}_a(\boldsymbol{x}, t) = \boldsymbol{u}_s(t) + \boldsymbol{X}^T(\boldsymbol{r}(\boldsymbol{x}))\boldsymbol{\omega}_s(t) \,. \tag{19}$$

3. Numerical method

In this section, we first discretize the governing equations in space to obtain time-dependent semi-discrete equations. The fluid equations are discretized using the 2D discrete streamfunction formulation developed by Colonius and Taira [3]. The semi-discrete equations are further discretized in time and coupled with the equations of motion integrated in time. The fully discrete algebraic equations are solved by a projection technique associated with the block-LU decomposition.

3.1. Spatial discretization and accurate stress filter

Following Taira and Colonius [2], we consider the spatial discretization in the fluid domain on a two-dimensional unbounded uniform staggered Cartesian grid, and the spatial discretization on the immersed boundary on an evenly spaced grid. Moreover, all the grid spacings are set to be the same, i.e., $\Delta x = \Delta y = \Delta s$. We start with discretizing the equations of motion of the rigid body spatially as

$$M_e\left(\frac{d\boldsymbol{u}_s}{dt}+\boldsymbol{X}(\boldsymbol{\omega}_s)\boldsymbol{u}_s\right)=S_1W_1f_1+M_e\boldsymbol{a}\,, \tag{20}$$

$$\boldsymbol{I}_e\frac{d\boldsymbol{\omega}_s}{dt}+\boldsymbol{X}(\boldsymbol{\omega}_s)\boldsymbol{I}_e\boldsymbol{\omega}_s=X_1W_1f_1+M_e\boldsymbol{X}(\boldsymbol{r}_c)\boldsymbol{a}\,, \tag{21}$$

where f_1 are the spatially discrete surface stresses of the FSI body (the spatial discretization of $-\boldsymbol{f}(\boldsymbol{\chi}_1(s),t)$).

Since the surface stresses obtained by many immersed boundary methods contain spurious oscillations [27–29], we include an accurate stress filter, W_1, introduced by Goza et al. [29] in (20) and (21) to obtain the physically correct surface stress on the immersed boundary. W_1f_1 is a discretization of

$$\frac{\int_\Omega\int_{\Gamma_1}(-\boldsymbol{f}(\boldsymbol{\chi}_1(s)))\delta(\boldsymbol{x}-\boldsymbol{\chi}_1(s))\delta(\boldsymbol{\chi}_1(s)-\boldsymbol{x})\,ds\,d\boldsymbol{x}}{\int_{\Gamma_1}\delta(\boldsymbol{x}-\boldsymbol{\chi}_1(s))\,ds}\,. \tag{22}$$

The numerical delta function used in the present work is from Roma [31]. The specific form of W_1 can be found in reference [29]. We also note that W_1 is a diagonal matrix so that $W_1^T=W_1$. Moreover, the linear integration operator, S_1, is the spatial discretization of $\int_{\Gamma_1}(\cdot)\,ds$. The angular integration operator, X_1, is the spatial discretization of $\int_{\Gamma_1}\boldsymbol{X}(\boldsymbol{r}(\boldsymbol{\chi}_1(s)))(\cdot)\,ds$.

By defining $M=diag(M_e\boldsymbol{I}_3,\boldsymbol{I}_e)$ ($\boldsymbol{I}_3$ is a 3×3 identity matrix), $\lambda=(\boldsymbol{u}_s,\boldsymbol{\omega}_s)^T$, $Q=(S_1W_1,X_1W_1)^T$ and $R=(M_e\boldsymbol{a}-M_e\boldsymbol{X}(\boldsymbol{\omega}_s)\boldsymbol{u}_s,M_e\boldsymbol{X}(\boldsymbol{r}_c)\boldsymbol{a}-\boldsymbol{X}(\boldsymbol{\omega}_s)\boldsymbol{I}_e\boldsymbol{\omega}_s)^T$, (20) and (21) can be written as

$$M\frac{d\lambda}{dt}=Qf_1+R\,. \tag{23}$$

Next, we discretize the fluid equations spatially as

$$\frac{dq}{dt}=-G\Pi+N(q,q_a)+\frac{1}{Re}Lq-H_1f_1-H_2f_2\,, \tag{24}$$

$$Dq=0\,, \tag{25}$$

$$E_1q=W_1^TS_1^T\boldsymbol{u}_s+W_1^TX_1^T\boldsymbol{\omega}_s=Q^T\lambda\,, \tag{26}$$

$$E_2q=q_{B_2}\,, \tag{27}$$

where q and Π are the spatially discrete fluid flux and pressure. q_{B_2} is the spatial discretization of $\boldsymbol{u}_B(\boldsymbol{\chi}_2(s,t),t)$. G, D, and L are the discrete gradient, divergence, and Laplacian operators. $N(q,q_a)$ is the spatial discretization of the nonlinear term $\boldsymbol{X}(\boldsymbol{u}-\boldsymbol{u}_a(\boldsymbol{x},t))\boldsymbol{\omega}$. H_i and E_i are the discretizations of the regularization and interpolation operators with respect to Γ_i in (1), (3), and (4). Discrete operators and variables are scaled such that $D=-G^T$ and $H_i=E_i^T$ for computational efficiency. We note that W_1^T is included in both terms on the right-hand side of (26) in order to write the equations in a symmetric form later. Since both $S_1^T\boldsymbol{u}_s$ and $X_1^T\boldsymbol{\omega}_s$ have no spurious oscillations, W_1^T has no effect on the resulting fluxes.

Following Colonius and Taira [3], a discrete curl operator, C, which lies in the null space of the discrete divergence operator, D, is constructed to mimic the vector identities that the divergence of the curl of any vector field and the curl of the gradient of any scalar field are always zero, i.e., $DC=-(C^TG)^T=0$. By introducing the discrete streamfunction, s, such that $q=Cs$ and taking curl, C^T, of (24), the incompressibility constraint (25) is satisfied automatically and the $-G\Pi$ term in (24) can be dropped. The fluid equations can be written as

$$C^TC\frac{ds}{dt}=C^TN(q,q_a(x))+\frac{1}{Re}C^TLCs-C^TE_1^Tf_1-C^TE_2^Tf_2\,, \tag{28}$$

$$E_1Cs=Q^T\lambda\,, \tag{29}$$

$$E_2Cs=q_{B_2}\,. \tag{30}$$

(28) is nothing but the semi-discrete vorticity equation with immersed-boundary forcing in the body-fixed frame and can be easily modified from the original null-space-approach immersed boundary projection method developed by Colonius and Taira [3].

3.2. Temporal discretization and factorization procedure

For the temporal discretization of the governing equations, we integrate (23) and (28) numerically from time t_n to t_{n+1}. We use an Adams-Bashforth scheme for the R term in (23) and the nonlinear terms in (28), and a Crank-Nicolson method for the diffusive term in (28). Most importantly, since E_1 and W_1 are time-invariant in the body-fixed frame and C^T, S_1, and X_1 are independent of time, when integrating the Qf_1 term in equation (23) and the $-C^TE_1^Tf_1$ term in equation (28) at temporal discretization, we can pull those operators out of the time integrals and integrate f_1 directly. We can define the average immersed boundary surface stress between $[t_n,t_{n+1}]$, $\overline{f}_1^{n+1}\equiv\frac{1}{\Delta t}\int_{t_n}^{t_{n+1}}f_1dt$, and solve for $\overline{f}_1^{n+1}\Delta t$ in equations (23) and (28) instead. In other words, with the aid of the target-fixed frame, no approximations are made for the time

integrals of the FSI coupling forces during the time marching. Moreover, we evaluate (29) and (30) at t_{n+1} and use an implicit Euler method for $-C^T E_2^T f_2$ in (28) to obtain a symmetric fully-discrete equation. After the temporal discretization, the semi-discrete governing equations yield a symmetric fully-discrete linear system:

$$\begin{bmatrix} C^T AC & 0 & C^T E_1^T & C^T E_2^{n+1^T} \\ 0 & M & -Q & 0 \\ E_1 C & -Q^T & 0 & 0 \\ E_2^{n+1} C & 0 & 0 & 0 \end{bmatrix} \begin{pmatrix} s^{n+1} \\ \lambda^{n+1} \\ \overline{f}_1^{n+1} \Delta t \\ f_2^{n+1} \Delta t \end{pmatrix} = \begin{pmatrix} r_1^n \\ r_2^n \\ 0 \\ q_{B_2}^{n+1} \end{pmatrix} , \tag{31}$$

where

$$A = I - \frac{\Delta t}{2Re} L , \tag{32}$$

$$r_1^n = C^T \left(I + \frac{\Delta t}{2Re} L \right) C s^n + \frac{3\Delta t}{2} C^T N(q^n, q_a^n) - \frac{\Delta t}{2} C^T N(q^{n-1}, q_a^{n-1}) , \tag{33}$$

$$r_2^n = M\lambda^n + \frac{3\Delta t}{2} R^n - \frac{\Delta t}{2} R^{n-1} . \tag{34}$$

Since the simplicity of (31) is set up on the stationary FSI Lagrangian points in the target-fixed frame and rigid-body dynamics of the FSI body, the present method is restricted to FSI problems with a single FSI rigid body and other non-FSI rigid bodies undergo prescribed motions. Extension to deforming FSI body will result in coupling the fluid equations with a complex solid equation and moving the FSI Lagrangian points relative to the fluid grid. In that case, iterations for the positions of the FSI Lagrangian points are required and we no longer benefit from the choice of the target-fixed frame to obtain spatially fixed FSI forces.

We use the block-LU decomposition to factorize the linear system (31). The factored equations are given below:

$$\begin{bmatrix} C^T AC & 0 \\ 0 & M \end{bmatrix} \begin{pmatrix} s^* \\ \lambda^* \end{pmatrix} = \begin{pmatrix} r_1^n \\ r_2^n \end{pmatrix} , \tag{35}$$

$$[Q^T M^{-1} Q + P_{11}] \overline{f}_1^* \Delta t = E_1 C s^* - Q^T \lambda^* , \tag{36}$$

$$\left[P_{22}^{n+1} - P_{21}^{n+1} (Q^T M^{-1} Q + P_{11})^{-1} \ P_{12}^{n+1} \right] f_2^{n+1} \Delta t = E_2^{n+1} C s^* - q_{B_2}^{n+1} - P_{21}^{n+1} \overline{f}_1^* \Delta t , \tag{37}$$

$$\overline{f}_1^{n+1} \Delta t = \overline{f}_1^* \Delta t - [Q^T M^{-1} Q + P_{11}]^{-1} P_{12}^{n+1} f_2^{n+1} \Delta t , \tag{38}$$

$$\begin{pmatrix} s^{n+1} \\ \lambda^{n+1} \end{pmatrix} = \begin{pmatrix} s^* \\ \lambda^* \end{pmatrix} + \begin{pmatrix} -(C^T AC)^{-1} C^T \left(E_1^T \overline{f}_1^{n+1} \Delta t + E_2^{n+1^T} f_2^{n+1} \Delta t \right) \\ M^{-1} Q \overline{f}_1 \Delta t \end{pmatrix} , \tag{39}$$

where

$$P_{11} = E_1 C (C^T AC)^{-1} C^T E_1^T , \tag{40}$$

$$P_{12}^{n+1} = E_1 C (C^T AC)^{-1} C^T E_2^{n+1^T} , \tag{41}$$

$$P_{21}^{n+1} = E_2^{n+1} C (C^T AC)^{-1} C^T E_1^T , \tag{42}$$

$$P_{22}^{n+1} = E_2^{n+1} C (C^T AC)^{-1} C^T E_2^{n+1^T} . \tag{43}$$

The factored equations (35)-(39) are analogous to the fractional-step procedure for the Navier-Stokes equations [32]. Analogous fractional-step methods have been developed by Taira and Colonius [2] for rigid body undergoing prescribed motions, Lācis et al. [18] for rigid-body interacting with the flow, and Goza and Colonius [21] for flow-structure interaction of thin elastic structures. Our current method is approximate to Taira and Colonius [2] when there are only non-FSI bodies and Lācis et al. [18] when there is only FSI body, differing in that all variables in the target-fixed frame and the surface stresses of FSI body have been physically-corrected and time-averaged between each time step.

The physical interpretation of (35) is that a trial streamfunction and trial rigid-body kinematics are predicted by evolving the discrete fluid equations and the equations of motion in the absence of the immersed boundary forcing. In (36), a Poisson-like problem for the prediction of the surface stresses of FSI body is solved to enforce the no-slip condition and the rigid-body dynamics in the absence of non-FSI bodies. In (37), another Poisson-like problem for the surface stresses of non-FSI bodies is solved to enforce the no-slip condition. The influence of the prediction of the surface stresses of FSI body to non-FSI bodies has also been taken into account. Through the projection step shown in (38), the surface stresses of FSI body are updated to include the influence of the surface stresses of non-FSI bodies. Finally, in (39) the streamfunction and rigid-body kinematics are corrected through projections to remove the part of the trial solution that does not satisfy the constraints.

When we solve the trial streamfunction in (35), a multi-domain setting is used to account for the boundary condition at infinity (see details in reference [3]) and the Poisson-like problem $(C^T AC)^{-1}$ can be solved efficiently using the discrete

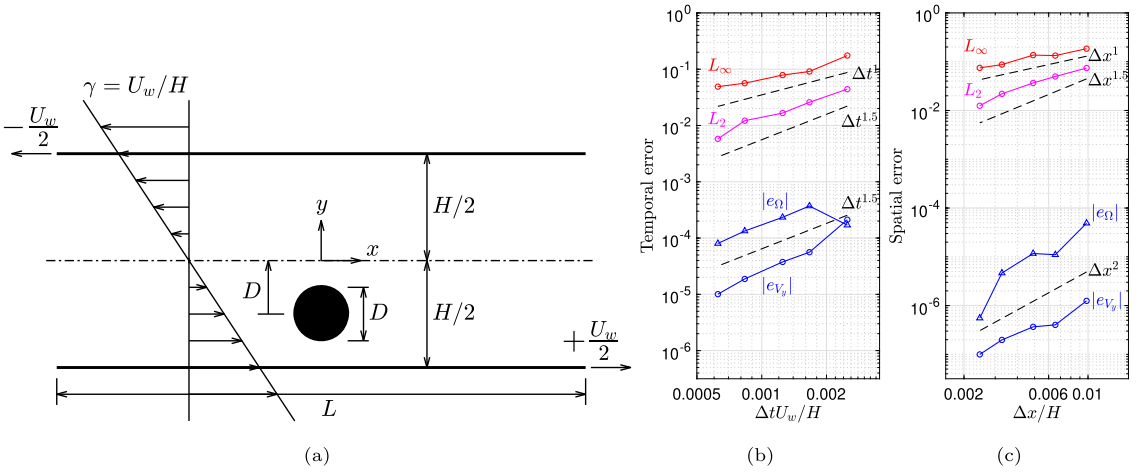

Fig. 1. (a) The schematic of a neutrally buoyant cylinder migrating in a planar Couette flow and (b) the temporal and (c) spatial convergence of the present method.

sine transform. In (36), since $Q^T M^{-1} Q + P_{11}$ is time-invariant and symmetric, it can be precomputed and solved efficiently (using, for example, the Cholesky decomposition). In (37), $P_{22}^{n+1} - P_{21}^{n+1}(Q^T M^{-1} Q + P_{11})^{-1} P_{12}^{n+1}$ is symmetric and can be solved efficiently using an iterative method such as Conjugate Gradient method.

We note that the interpolation operator E_2 depends on the positions of non-FSI rigid bodies in the target-fixed frame and is therefore time-dependent due to the relative motion between non-FSI bodies and the FSI body. Once $\lambda^{n+1} = (\boldsymbol{u}_s^{n+1}, \boldsymbol{\omega}_s^{n+1})$ is computed at each time step, the location of the center of mass and the rotation angle of the FSI rigid body in the laboratory frame can be integrated numerically as a post-processing step using an explicit scheme, like an Adams-Bashforth scheme. Then we move non-FSI rigid bodies accordingly in the target-fixed frame and update E_2^{n+1} and $q_{B_2}^{n+1}$.

4. Verifications and validations

4.1. A neutrally buoyant cylinder migrating in a planar Couette flow

In order to validate the present method, we consider a test problem of a neutrally buoyant cylinder migrating in a planar Couette flow. As shown in Fig. 1a, a neutrally buoyant cylinder with radius D is initially at rest and released at $y = -D$. The cylinder is free to translate and rotate. In order to mimic a planar Couette flow in a channel of height H, two horizontal flat plates with length L are placed at $y = \pm H/2$ in a simple shear flow. The channel height is $H = 4.0D$ and the plate length is $L = 15.0D$. The shear rate of the simple shear flow is $\gamma = U_w/H$ and the upper and lower plates are moving in x-direction with velocities $-U_w/2$ and $U_w/2$, respectively. This configuration is also used by Lācis et al. [18], Feng et al. [33], and Vasseur and Cox [34].

In the following simulations, the characteristic length is the channel height H and the characteristic velocity is U_w. With the present target-fixed IB method, simulations are done in a frame of reference fixed on the targeted FSI cylinder. The upper and lower non-FSI plates are moving in correspondence to the kinematics of the cylinder in the laboratory frame. We use a multi-domain setting of the first domain size $4H \times 2H$ and the number of domains $N_g = 4$. As shown in (9) and (10), M_e and $\boldsymbol{I}_e$ is singular when $\rho = \rho_s/\rho_f = 1$, where ρ_s is the solid density. Therefore, we set the background acceleration $\boldsymbol{a} = 0$ and use a slightly larger density ratio $\rho = 1.01$, which corresponds to a small effective density ratio $\rho_e = \rho - 1 = 0.01$, to simulate the flow interacting with a neutrally buoyant cylinder. In order to compare the numerical solution with the works by Lācis et al. [18] and Feng et al. [33], a Reynolds number $Re_H = U_w H/\nu_f = 40$ is selected. Feng et al. [33] used a finite element solver on a body-fitted mesh and Lācis et al. [18] used an implicitly-coupled immersed boundary projection method in a finite domain of size $40H \times H$ with velocity Dirichlet boundary conditions being specified.

First we focus on the convergence properties of the present method when dynamics of FSI bodies and kinematics of non-FSI bodies are coupled with the fluid solver. In order to investigate the temporal convergence, simulations with dimensionless time steps $\Delta t U_w/H$ ranging from 3.125×10^{-4} to 2.5×10^{-3} are examined. The grid spacing is adjusted correspondingly to hold CFL numbers around 0.25. The simulations are carried out until $tU_w/H = 0.25$. The simulation with the smallest Δt is used as reference and its vorticity field is interpolated using a cubic interpolation on coarser grid to compute error in the vorticity field, i.e., $e_{ij} = \omega_{ij} - \tilde{\omega}_{ij,\mathrm{ref}}$. The infinity-norm L_∞ of the vorticity error field is defined as $\max(|e_{ij}|)$ and 2-norm L_2 of the vorticity error field is defined as $\sqrt{\sum(e_{ij}^2 \Delta x^2)}$. Errors in the angular velocity and the vertical velocity of the cylinder at $tU_w/H = 0.25$, $|e_\Omega|$ and $|e_{V_y}|$, are calculated using the differences between values in the reference simulation and values in simulation with a coarser grid. The temporal convergences of L_∞, L_2, $|e_\Omega|$, and $|e_{V_y}|$ are shown in Fig. 1b. We can see that the convergence rate in time is around 1 in L_∞ and around 1.5 in L_2, $|e_\Omega|$, and $|e_{V_y}|$.

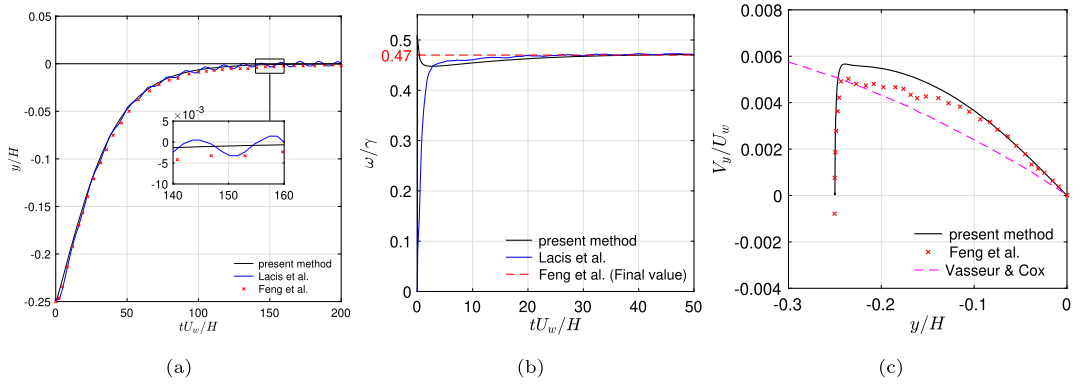

Fig. 2. The histories of (a) the vertical displacement and (b) the angular velocity of the neutrally buoyant cylinder, and (c) the phase space of the vertical displacement of the neutrally buoyant cylinder. Only the final value of the ratio of the angular velocity to the shear rate was reported by Feng et al. [33].

To investigate the spatial convergence, we use a very small time step of $\Delta t U_w/H = 10^{-4}$ and several grid spacings $\Delta x/H$ ranging from 0.00125 to 0.01. We carry out the simulations until $tU_w/H = 0.01$. Similarly, the simulation with the finest grid is used as reference to compute L_∞ and L_2 of the vorticity error, $|e_\Omega|$, and $|e_{V_y}|$. As shown in Fig. 1c, the convergence rate in space is around 1 in L_∞, around 1.5 in L_2, and around 2 in $|e_\Omega|$ and $|e_{V_y}|$.

In the following simulation we use a moderate grid spacing $\Delta x = 0.01H$ and a moderate time step $\Delta t = 0.005H/U_w$. Figs. 2a and 2b show the histories of the vertical displacement and the angular velocity of the neutrally buoyant cylinder, respectively. The results agree well with Lācis et al. [18] and Feng et al. [33]. The cylinder is initially at rest. Once the cylinder is released, it migrates downstream and toward the center of the channel and its rotating rate increase rapidly to a final value about 47% of the shear rate of the simple shear flow. According to Lācis et al. [18], the small oscillations in their trajectory (Fig. 2a) are due to the fact that the Lagrangian points are moving relative to the fluid grid during the migration. They referred this oscillating behavior as "grid locking", where similar behavior was also observed in IB simulations by Breugem [15]. Due to the target-fixed nature of the present method, we avoid generating the "grid-locking" oscillations. Fig. 2c shows the vertical displacement and the velocity of the neutrally buoyant cylinder in the phase space. The numerical result of Feng et al. [33] and the analytical result of Vasseur and Cox [34] for a small sphere migrating in a slow flow are also shown for comparison. Besides the initial transients, which are not being addressed by Vasseur and Cox [34], the trends are alike and the computational results agree well when the cylinder moves closer to the center of the channel.

4.2. Freely falling/rising circular cylinders

We consider a two-dimensional incompressible flow around a circular cylinder freely falling or rising under the gravitational pull, depending on the density of the cylinder, as shown in Fig. 3a. The characteristic length is the cylinder diameter D and the characteristic velocity is the vertical terminal velocity V_{term}. The origin of the body-fixed frame is placed at the center of the cylinder and the axes of the body-fixed frame are initially aligned in the horizontal and vertical directions. In order to validate our method, we compare the numerical solution with the works by Namkoong et al. [35] and Lācis et al. [18]. Namkoong et al. [35] used a finite element method with implicit coupling and adaptive body-fitted mesh to simulate the flow in an infinite fluid, and the resolution in the wake was refined. Lācis et al. [18] used an immersed boundary projection method in a finite domain of size $10D \times 100D$ (with its origin at the center of the domain) with a time-lagged interpolation and an added-mass correction. A Reynolds number $Re = V_{\text{term}} D/\nu_f = 156$ and a Galilei number $Ga = \sqrt{|\rho_s/\rho_f - 1|gD^3}/\nu_f = 138$ were selected, where g is the gravitational acceleration. Again, small effective density ratios $\rho_e = \rho - 1 = \pm 0.01$ were selected for freely falling/rising cylinders. Thus, a solid-to-fluid density ratio $\rho_s/\rho_f = 1.01$ is used for a freely falling cylinder and $\rho_s/\rho_f = 0.99$ for a freely rising cylinder.

The multi-domain setting in our simulation is of the first domain size $4D \times 4D$ and the number of domains $N_g = 6$. The finest grid spacing is $\Delta x = 0.04D$ and the CFL number $V_{\text{term}}\Delta t/\Delta x$ is set to be less than 0.4. Fig. 3b and Fig. 3c show, respectively, the comparisons of the vertical and transversal velocity of the freely falling cylinder using the present method with that of reference [35] and [18]. Fig. 4 shows the vorticity fields around the freely falling and rising cylinders at $t = 8$ and 92. At an early time $t = 8$, the cylinder wake is symmetric for both freely falling and rising cylinders. At a late time $t = 92$, vortex shedding occurs in the wake for both cases. We can see from Fig. 3b and Fig. 3c that the vertical velocity agrees well in early development and later stationary oscillation, and that the transversal velocity reaches the same stationary oscillation at a later time. During the transient regime, the wake instability develops, breaks the symmetry of cylinder wake, and results in stationary vortex shedding (Fig. 4a). The difference in the onset of wake instability observed in Fig. 3b is due to the different rate at which numerical error accumulates.

In Table 1, we compare the Strouhal number, the drag coefficient, and the amplitude of lift coefficient with Lācis et al. [18] and Namkoong et al. [35]. The Strouhal number is defined as $St = f_L D/V_{\text{term}}$, where f_L is frequency of os-

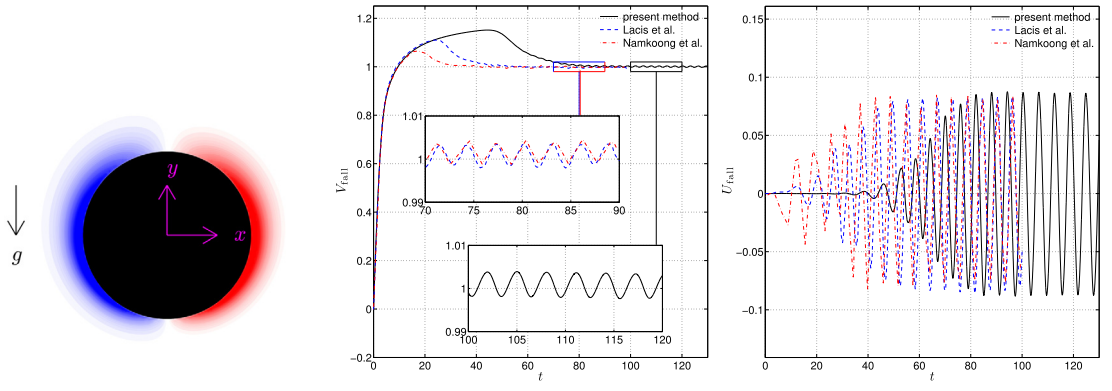

Fig. 3. (a) The schematic of a freely falling/rising cylinder and (b) the vertical and (c) transversal velocity of the freely falling cylinder with $\rho_s/\rho_f = 1.01$ at $Re = 156$ and $Ga = 138$. Velocities from Namkoong et al. [35] and Lācis et al. [18] are reported only up to $t = 100$.

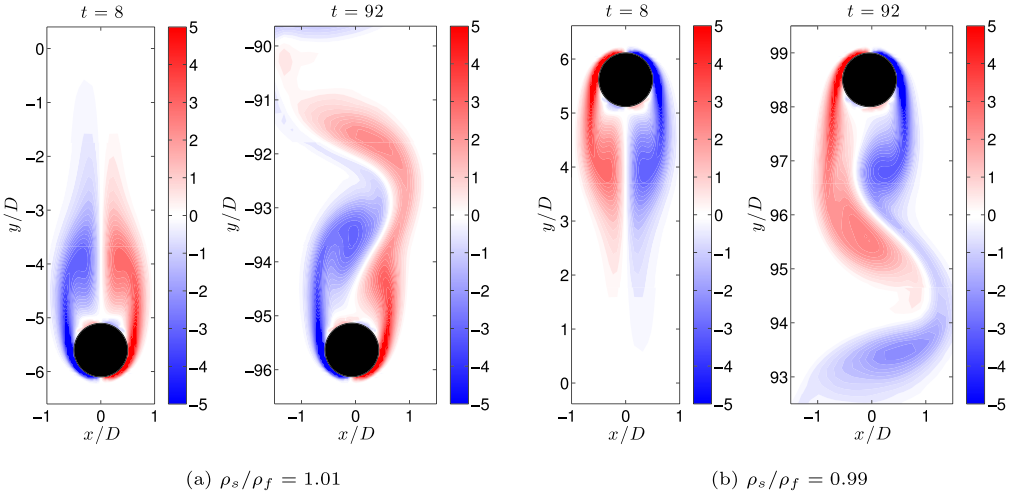

Fig. 4. The vorticity fields of (a) a freely falling cylinder ($\rho_s/\rho_f = 1.01$) and (b) a freely rising cylinder ($\rho_s/\rho_f = 0.99$) at $t = 8$ and 92, $Re = 156$, and $Ga = 138$.

Table 1
Flow characteristics of freely falling and rising cylinders with density ratios $\rho_s/\rho_f = 1.01$ and 0.99, respectively, at $Re = 156$ and $Ga = 138$. Values of Strouhal number, drag coefficient, and amplitude of lift coefficient are compared. We note that only the Strouhal number is reported for the freely rising cylinder in Namkoong et al. [35].

	Falling			Raising		
	St	C_D	$\max\|C_L\|$	St	C_D	$\max\|C_L\|$
Present method	0.1640	1.23	0.12	0.1640	1.23	0.12
Lācis et al. [18]	0.17185	1.29	0.14	0.17188	1.29	0.14
Namkoong et al. [35]	0.16840	1.23	0.15	0.16870	–	–

cillations in lift force due to vortex shedding. The lift and drag coefficients are scaled by $\rho_f V_{\text{term}}^2 D/2$. Again, satisfactory agreements are observed, especially with the results of Namkoong et al. [35], which are also simulated in an infinite fluid domain. We note that both [35] and [18] reported a slightly higher Strouhal number for a freely rising cylinder than a freely falling cylinder, while the Strouhal numbers for freely falling and rising cylinders are the same using the present method.

5. Conclusion

We presented an immersed boundary projection method that solves the FSI problems involving a FSI rigid body and a number of non-FSI rigid bodies. The method is formulated in a frame of reference fixed on the targeted FSI rigid body in order to advance the FSI system non-iteratively and obtain spatially fixed FSI forces. The fluid solver of the present method

retains mathematical and computational simplicity using the null-space approach and couples with dynamics of the FSI body implicitly to ensure numerical stability for wide ranges of solid-to-fluid mass ratios. By solving for the time average of the spatially fixed FSI forces between each time step, FSI force terms can be advanced in time without truncation errors. Moreover, the effect of the fictitious fluid flow inside the FSI body has also been taken into account to obtain accurate rigid body dynamics. The method further imposes the physical correct surface stresses by applying an accurate stress filter. We derive the developed method for general 3D rigid bodies and solve it efficiently by the block-LU decomposition. The method is validated for a neutrally buoyant cylinder migrating in a planar Couette flow and 2D flow around a freely falling or rising cylindrical rigid body.

CRediT authorship contribution statement

Tzu-Yuan Lin: Data curation, Investigation, Methodology, Software, Validation, Writing – original draft, Writing – review & editing. **Hsin-Yu Hsieh:** Data curation, Investigation, Software, Validation, Visualization, Writing – original draft. **Hsieh-Chen Tsai:** Conceptualization, Funding acquisition, Methodology, Project administration, Supervision, Writing – review & editing.

Declaration of competing interest

The authors declare that they have no known competing financial interests or personal relationships that could have appeared to influence the work reported in this paper.

Acknowledgements

This research was supported by a grant from the Ministry of Science and Technology, Taiwan (Grant No. MOST 108-2636-E-002-010).

Appendix A. Alternative form of the incompressible Navier-Stokes equations in a non-inertial frame of reference

We start with the dimensionless incompressible Navier-Stokes equations and the dimensionless continuity equation in a non-inertial frame of reference that translates with velocity $\boldsymbol{U}(t)$ and rotates with angular velocity $\boldsymbol{\Omega}(t)$ about a center of rotation

$$\frac{\partial \boldsymbol{u}_n}{\partial t} + (\boldsymbol{u}_n \cdot \nabla)\,\boldsymbol{u}_n = -\nabla p + \frac{1}{Re}\nabla^2 \boldsymbol{u}_n + \boldsymbol{a} - \frac{d\boldsymbol{U}}{dt} - \boldsymbol{\Omega} \times \boldsymbol{U} - \frac{d\boldsymbol{\Omega}}{dt} \times \boldsymbol{r} - 2\,\boldsymbol{\Omega} \times \boldsymbol{u}_n - \boldsymbol{\Omega} \times (\boldsymbol{\Omega} \times \boldsymbol{r})\ , \tag{44}$$

$$\nabla \cdot \boldsymbol{u}_n = 0\ . \tag{45}$$

With the add of the facts that $\boldsymbol{a} = \nabla(\boldsymbol{a} \cdot \boldsymbol{r})$, $\frac{d\boldsymbol{\Omega}}{dt} \times \boldsymbol{r} = \frac{d}{dt}(\boldsymbol{\Omega} \times \boldsymbol{r}) - \nabla[(\boldsymbol{\Omega} \times \frac{\partial \boldsymbol{r}}{\partial t}) \cdot \boldsymbol{r}]$, $\boldsymbol{\Omega} \times (\boldsymbol{\Omega} \times \boldsymbol{r}) = -\nabla\left(\frac{1}{2}|\boldsymbol{\Omega} \times \boldsymbol{r}|^2\right)$ and $\boldsymbol{\Omega} \times \boldsymbol{U} = -\nabla[(\boldsymbol{\Omega} \times \boldsymbol{r}) \cdot \boldsymbol{U}]$, and the vector identity $(\boldsymbol{u}_n \cdot \nabla)\,\boldsymbol{u}_n = \nabla\left(\frac{1}{2}|\boldsymbol{u}_n|^2\right) - \boldsymbol{u}_n \times \boldsymbol{\omega}_n$, (44) can be written as

$$\frac{\partial \boldsymbol{u}_n}{\partial t} = -\nabla \Pi + \boldsymbol{u}_n \times \boldsymbol{\omega}_n + \frac{1}{Re}\nabla^2 \boldsymbol{u}_n - \frac{d\boldsymbol{U}}{dt} - \frac{d}{dt}(\boldsymbol{\Omega} \times \boldsymbol{r}) - 2\,\boldsymbol{\Omega} \times \boldsymbol{u}_n\ , \tag{46}$$

where

$$\Pi = p + \frac{1}{2}|\boldsymbol{u}_n|^2 - (\boldsymbol{\Omega} \times \boldsymbol{r}) \cdot \boldsymbol{U} - \frac{1}{2}|\boldsymbol{\Omega} \times \boldsymbol{r}|^2 - \left(\boldsymbol{a} + \boldsymbol{\Omega} \times \frac{\partial \boldsymbol{r}}{\partial t}\right) \cdot \boldsymbol{r}\ . \tag{47}$$

We introduce the change of variables in velocity and vorticity

$$\boldsymbol{u} = \boldsymbol{u}_n + \boldsymbol{U} + \boldsymbol{\Omega} \times \boldsymbol{r} \equiv \boldsymbol{u}_n + \boldsymbol{U}_a\ , \tag{48}$$

$$\boldsymbol{\omega} = \nabla \times \boldsymbol{u} = \boldsymbol{\omega_n} + 2\,\boldsymbol{\Omega}\ , \tag{49}$$

where $\boldsymbol{U}_a = \boldsymbol{U} + \boldsymbol{\Omega} \times \boldsymbol{r}$ is the velocity of a fixed point in the non-inertial frame of reference relative to the inertial frame of reference, and $\boldsymbol{\omega}_n = \nabla \times \boldsymbol{u}_n$ is the fluid vorticity in the non-inertial frame. We can treat $\boldsymbol{u}$ and $\boldsymbol{\omega}$ as the fluid velocity and vorticity in the inertial frame, respectively. (45) and (46) can be written as

$$\frac{\partial \boldsymbol{u}}{\partial t} = -\nabla \Pi + (\boldsymbol{u} - \boldsymbol{U}_a) \times \boldsymbol{\omega} + \frac{1}{Re}\nabla^2 \boldsymbol{u}\ , \tag{50}$$

$$\nabla \cdot \boldsymbol{u} = 0\ , \tag{51}$$

where

$$\Pi = p + \frac{1}{2}|\boldsymbol{u} - \boldsymbol{U}_a|^2 - \frac{1}{2}|\boldsymbol{U}_a|^2 + \frac{1}{2}|\boldsymbol{U}|^2 - \left(\boldsymbol{a} + \boldsymbol{\Omega} \times \frac{\partial \boldsymbol{r}}{\partial t}\right) \cdot \boldsymbol{r} \,. \tag{52}$$

(50) and (51) are not the standard non-inertial-frame form of equations, but are computationally convenient to implement because they render the governing equations free from the body forces (e.g. centrifugal forces, Coriolis forces, etc), and because the dependent variables decay at infinity.

References

[1] C.S. Peskin, Flow patterns around heart valves: a numerical method, J. Comput. Phys. 10 (2) (1972) 252–271.
[2] K. Taira, T. Colonius, The immersed boundary method: a projection approach, J. Comput. Phys. 225 (2) (2007) 2118–2137.
[3] T. Colonius, K. Taira, A fast immersed boundary method using a nullspace approach and multi-domain far-field boundary conditions, Comput. Methods Appl. Mech. Eng. 197 (25) (2008) 2131–2146.
[4] K. Taira, T. Colonius, Effect of tip vortices in low-Reynolds-number poststall flow control, AIAA J. 47 (3) (2009) 749–756.
[5] K. Taira, T. Colonius, Three-dimensional flows around low-aspect-ratio flat-plate wings at low Reynolds numbers, J. Fluid Mech. 623 (2009) 187–207.
[6] K. Taira, C.W. Rowley, T. Colonius, D.R. Williams, Lift enhancement for low-aspect-ratio wings with periodic excitation, AIAA J. 48 (8) (2010) 1785–1790.
[7] K.K. Chen, T. Colonius, K. Taira, The leading-edge vortex and quasi-steady vortex shedding on an accelerating plate, Phys. Fluids 22 (3) (2010) 033601.
[8] J. Choi, T. Colonius, D.R. Williams, Surging and plunging oscillations of an airfoil at low Reynolds number, J. Fluid Mech. 763 (2015) 237–253.
[9] X.B. Li, M.L. Hunt, T. Colonius, A contact model for normal immersed collisions between a particle and a wall, J. Fluid Mech. 691 (2012) 123–145.
[10] H.-C. Tsai, T. Colonius, Coriolis effect on dynamic stall in a vertical axis wind turbine, AIAA J. 54 (1) (2016) 216–226.
[11] M. Uhlmann, An immersed boundary method with direct forcing for the simulation of particulate flows, J. Comput. Phys. 209 (2) (2005) 448–476.
[12] I. Borazjani, L. Ge, F. Sotiropoulos, Curvilinear immersed boundary method for simulating fluid structure interaction with complex 3d rigid bodies, J. Comput. Phys. 227 (16) (2008) 7587–7620.
[13] J.D. Eldredge, Dynamically coupled fluid-body interactions in vorticity-based numerical simulations, J. Comput. Phys. 227 (21) (2008) 9170–9194.
[14] T. Kempe, J. Fröhlich, An improved immersed boundary method with direct forcing for the simulation of particle laden flows, J. Comput. Phys. 231 (9) (2012) 3663–3684.
[15] W.-P. Breugem, A second-order accurate immersed boundary method for fully resolved simulations of particle-laden flows, J. Comput. Phys. 231 (13) (2012) 4469–4498.
[16] J. Yang, F. Stern, A non-iterative direct forcing immersed boundary method for strongly-coupled fluid-solid interactions, J. Comput. Phys. 295 (2015) 779–804.
[17] C. Wang, J.D. Eldredge, Strongly coupled dynamics of fluids and rigid-body systems with the immersed boundary projection method, J. Comput. Phys. 295 (2015) 87–113.
[18] U. Lācis, K. Taira, S. Bagheri, A stable fluid–structure-interaction solver for low-density rigid bodies using the immersed boundary projection method, J. Comput. Phys. 305 (2016) 300–318.
[19] X. Zheng, Q. Xue, R. Mittal, S. Beilamowicz, A coupled sharp-interface immersed boundary-finite-element method for flow-structure interaction with application to human phonation, J. Biomech. Eng. 132 (11) (2010) 111003.
[20] I. Borazjani, Fluid-structure interaction, immersed boundary-finite element method simulations of bio-prosthetic heart valves, Comput. Methods Appl. Mech. Eng. 257 (2013) 103–116.
[21] A. Goza, T. Colonius, A strongly-coupled immersed-boundary formulation for thin elastic structures, J. Comput. Phys. 336 (2017) 401–411.
[22] L.P. Tosi, T. Colonius, Modeling and simulation of a fluttering cantilever in channel flow, J. Fluids Struct. 89 (2019) 174–190.
[23] F. Sotiropoulos, X. Yang, Immersed boundary methods for simulating fluid-structure interaction, Prog. Aerosp. Sci. 65 (2014) 1–21.
[24] W. Kim, H. Choi, Immersed boundary methods for fluid-structure interaction: a review, Int. J. Heat Fluid Flow 75 (2019) 301–309.
[25] S. Schwarz, T. Kempe, J. Fröhlich, A temporal discretization scheme to compute the motion of light particles in viscous flows by an immersed boundary method, J. Comput. Phys. 281 (2015) 591–613.
[26] W. Kim, I. Lee, H. Choi, A weak-coupling immersed boundary method for fluid-structure interaction with low density ratio of solid to fluid, J. Comput. Phys. 359 (2018) 296–311.
[27] X. Yang, X. Zhang, Z. Li, G.-W. He, A smoothing technique for discrete delta functions with application to immersed boundary method in moving boundary simulations, J. Comput. Phys. 228 (20) (2009) 7821–7836.
[28] J.H. Seo, R. Mittal, A sharp-interface immersed boundary method with improved mass conservation and reduced spurious pressure oscillations, J. Comput. Phys. 230 (19) (2011) 7347–7363.
[29] A. Goza, S. Liska, B. Morley, T. Colonius, Accurate computation of surface stresses and forces with immersed boundary methods, J. Comput. Phys. 321 (2016) 860–873.
[30] B. Kallemov, A. Bhalla, B. Griffith, A. Donev, An immersed boundary method for rigid bodies, Commun. Appl. Math. Comput. Sci. 11 (1) (2016) 79–141.
[31] A.M. Roma, C.S. Peskin, M.J. Berger, An adaptive version of the immersed boundary method, J. Comput. Phys. 153 (2) (1999) 509–534.
[32] J.B. Perot, An analysis of the fractional step method, J. Comput. Phys. 108 (1) (1993) 51–58.
[33] J. Feng, H. Hu, D. Joseph, Direct simulation of initial value problems for the motion of solid bodies in a Newtonian fluid. Part 2. Couette and Poiseuille flows, J. Fluid Mech. 277 (271) (1994) 271–301.
[34] P. Vasseur, R.G. Cox, The lateral migration of a spherical particle in two-dimensional shear flows, J. Fluid Mech. 78 (1976) 385.
[35] K. Namkoong, J.Y. Yoo, H.G. Choi, Numerical analysis of two-dimensional motion of a freely falling circular cylinder in an infinite fluid, J. Fluid Mech. 604 (2008) 33–53.